

We are IntechOpen, the world's leading publisher of Open Access books Built by scientists, for scientists

4,800

Open access books available

122,000

International authors and editors

135M

Downloads

Our authors are among the

154

Countries delivered to

TOP 1%

most cited scientists

12.2%

Contributors from top 500 universities



WEB OF SCIENCE™

Selection of our books indexed in the Book Citation Index
in Web of Science™ Core Collection (BKCI)

Interested in publishing with us?
Contact book.department@intechopen.com

Numbers displayed above are based on latest data collected.
For more information visit www.intechopen.com



The Special Case of Sea Mines

Olga Lucia Lopera Tellez, Alexander Borghgraef and
Eric Mersch

Additional information is available at the end of the chapter

<http://dx.doi.org/10.5772/66994>

Abstract

In this chapter, work carried out at the Royal Military Academy regarding sea mines and mine countermeasures is summarized. Three sensors used for the detection and identification of sea mines are studied here: sonar, gradiometer and infrared camera. These sensors can be applied to detect different types of sea mines. Some signal and image processing techniques developed to extract relevant information for the detection of underwater objects are presented in this chapter. These techniques are validated using data collected in the frame of different European and NATO projects.

Keywords: sea mines, mine countermeasures, sonar, gradiometer, infrared camera

1. Introduction

Land mines and sea mines have more in common than one could think. Generally speaking, land/sea mines are intended to prevent the use of or passage through an area in land or sea. Considering that maritime areas provide a vital dimension of the world's economy (90% of global trade and about half of the world's oil are transported by sea), sea mines are a complex hazard of international concern.

Defensively, military forces deploy sea mines to discourage undesired entrance into territorial waters. Offensively, sea mines are deployed to hobble a target's naval assets or channel an enemy through a designed route. Mine warfare is an old military technique and has been applied in many conflicts since the nineteenth century. Like land mines, sea mines can still be active after many years of being deployed. More than 550,000 sea mines were laid during World War II (WW-II); some of them were removed after the conflict but part of them were missed [1, 2]. The legacy of recent conflicts in the north of Africa means that even today, sea mines can be laid in European waters (and in any critical maritime space where vital resources are transported) and

therefore remain a very real threat to shipping, sailors and any maritime exploitation of ocean and coastal resources.

To address this problem, governments around the world have traditionally relied on a standing mine countermeasures (MCM) force, which involves both passive and active tactics. Passive countermeasures entail changing the specific target vessel characteristics or signatures, since these trigger sea mines (see next section for more information about sea mines). These might include building vessels with fibreglass or wood instead of steel or even attempting to alter a steel vessel's magnetic field through degaussing. Alternatively, active countermeasures aim to discover mines using specially designed ships or platforms for the purpose of either avoiding or destroying them. Mine sweeping and mine hunting are two of these measures. Mine sweeping uses either a contact sweep, a wire dragged through the water by one or two ships to cut the mooring wire of floating mines, or a distance sweep that mimics a ship to detonate the mines. Mine hunting is very different from sweeping. It requires searching for all the mines in an area before disposing them. The latter is generally decomposed in four stages:

1. Detection: finding targets or contacts from signals of different sensors (e.g. acoustic, magnetic).
2. Classification: determining if the contact is mine-like or friendly object.
3. Identification: using additional information (e.g. from a diver or autonomous underwater vehicle (AUV)-based camera) to validate the classification result.
4. Disposal: neutralizing the mine.

As mines have become smarter, MCM have become more complex and sophisticated. Modern navies employ an array of different mine warfare countermeasures. The trend in mine hunting operations goes towards keeping the human operators out of the minefield. In order to achieve this, modern MCM forces use (semi)autonomous platforms (e.g., AUV, remotely operating vehicles [ROV], unmanned surface/underwater vehicles [USV/UUV]), equipped with high-resolution (HR) sensors (e.g. sonars, magnetometers, optical cameras) and employing computer-aided detection (CAD) and classification (CAC) algorithms as well as automated target recognition (ATR) processes.

Not only high-tech hardware and software are developed for mine hunting operations, but biotechnology is also applied. Just as dogs and rodents can be trained to detect land mines, maritime mammals such as dolphins are trained by the United States and Soviet navies to detect sea mines while keeping the deminer out of the minefield. Dolphins are trained to detect and mark the location of tethered mines floating off the bottom, mines on the sea floor or mines buried in sediment. They learn to use their natural echolocation bio-sonar to find a target and to report back to their handler, giving particular responses to communicate whether a target is detected. The handler then sends the dolphin to mark the location of the object by releasing a buoy. The US Navy reported that mine-clearance dolphins were deployed in the Persian Gulf during the Iraq war in 2003. The Navy said these dolphins were effective in helping to detect more than 100 sea mines [3].

This chapter reviews research carried out at the Royal Military Academy addressing the applicability of acoustic, magnetic and optical sensors used in mine hunting operations and introduce some of the challenges these techniques encounter in order to detect and classify sea mines.

2. Types of sea mines

Sea mines typically are explosive devices designed in different forms whose dimensions can vary from around 50 cm up to almost 3 m and can contain from 50 kg to over 1000 kg of high explosives. Aside from their dimensions and explosive charges, mines can be further categorized by their method of deployment, position in the water column and method of actuation (or detonation) [2].

Sea mines can be laid in many different ways, which depend on the size of the mine itself. Certain conventional surface vessels, e.g. war vessels and patrol vessels, can have sea mines deploying capabilities. Some smaller, unusual surface vehicles (e.g. smaller fishing boat) could drop sea mines too. They can also be deployed from air using either fixed or rotary wing aircraft or deployed underwater using the torpedo tubes of submarines.

Depending on the type, sea mines can be positioned at different altitudes in the water column. The most common type of sea mines deployed during both World War I (WW-I) and WW-II was drifting mines. They float freely on the water surface following the direction of water currents or winds. The latter have been banned by international law for over 70 years; however, some countries still use them in their defensive/offensive strategies in conflicts since 1980 [2]. Highly versatile drifting mines can be deployed by small boats, warships or aircraft. Drifting sea mines can be activated remotely or by contact.

As their name suggests, bottom sea mines stay on the seafloor utilizing negative buoyancy or are partially/totally buried at the bottom of the sea. Most of these sea mines are influence mines; a few ones can also be activated remotely or by contact. Since they rest on the bottom of the sea, bigger explosive charges (around 1000 kg) can easily fit inside them. To be able to sense vessels on the surface and reach the ship's hull floating near the surface with their explosive energy, bottom sea mines tend to be used in relatively shallow water (less than 50 m). Bottom mines are generally laid by aircraft or submarine.

In contrast with bottom or drifting sea mines, moored sea mines must maintain buoyancy to float at certain water depths. In order to achieve this, part of their structure must be designated to maintaining their buoyancy and therefore the weight and size are key factors in their design. Moored sea mines are filled with smaller amounts of explosives than bottom sea mines. Additionally, they can be tethered to allow for various altitudes in the water column. The latter are by far the most sophisticated and expensive types of sea mines. Deployed most commonly by conventional surface ships, moored mines can be contact, influence or remote-controlled mines.

The most easy-to-use mines, contact sea mines, actuate when a vessel physically comes into contact with (or very close to) the mine in the water. Contact sea mines have been fitted with many ingenious anti-sweep devices including explosive charges to cut sweeping wires and ratchet devices that enable a sweep wire to pass through the mooring cable without cutting it [2]. Contact mines are available at costs between US\$2000 and US\$15,000 [1].

Influence sea mines are becoming more sophisticated, complex and technically advanced. These categories of sea mines do not need physical pressure to detonate. Instead, these mines hold different kinds of sensors that can respond to different vessel signatures. The latter sense

magnetic, acoustic, pressure or underwater electrical potential signals. Originally, magnetic sea mines used the vertical component of the vessel’s magnetic field to activate themselves when a given field density was reached. During the 1930s, magnetic mines worked off the horizontal component of the ship’s magnetic field [2]. This apparently insignificant change made it possible to design a mine fuse which responded to the rate of change of field strength rather than absolute field strength. This made defence against magnetic sea mines by degaussing and magnetic sweeping procedures far less effective. Magnetic mines are available at costs between US\$10,000 and US\$25,000 [1].

Due to the vessel’s machinery, the design of the hull and the propellers (and many other factors), all ships and submarines have a specific acoustic signature. This principle is used in the fabrication of acoustic sea mines. Delay clocks can be included to leave the sea mine inert (and thus unsweepable) for some days after it has been deployed, while the incorporation of counters means that the sea mine will only be detonated after a certain number of impulses have been received. This means a sweeper would have to make a large number of passes over a suspected field before it could be sure that all the mines within the field had been exploded. The cost of acoustic sea mines differs dramatically depending on the capability of its system (bandwidth). They are available at costs between US\$50,000 and US\$150,000 [1].

Pressure mines are invariably bottom mines since they measure the absolute drop in pressure associated with the difference between the known pressure due to water depth and the depth of water under the hull of a passing ship. This differential is directly related to the depth at which the mine is situated. Pressure mines are inevitably unsweepable, are shallow-water inshore weapons and are specifically intended to destroy amphibious craft. They are located in such shallow water (even surf zone) that even minute pressure signatures would detonate them. Pressure mines have been adopted for an entire generation of small anti-invasion mines [2]. They are available at costs between US\$25,000 and US\$50,000 [1].

In this chapter, focus will be made on bottom and drifting mines. **Table 1** lists some of them with their characteristics and dimensions.

Mine name	Shape	Weight (in air, kg)	Dimensions (mm)	
Murena	Cylindrical	780	Length	2096
			Diameter	533
Manta	Truncated cone	220	Height	440
			Diameter	980 (max)
Rockan	Wedge	190	Length	1020
			Height:	385
			Width	80

Table 1. Some bottom type mines and their characteristics.

3. Sonar applied to mine hunting

3.1. Underwater sonar principles and limitations

SONAR is an acronym for SOund Navigation And Ranging, and its basic principle is to locate objects by using acoustic (or sound) waves. Sound is a series of pressure perturbations that travel as a wave and exhibit phenomena like reflection, diffraction and interference. These acoustic vibrations can be characterized by their sound velocity c , frequency f and wavelength $\lambda = c / f$ [4].

The propagation velocity of an acoustic wave is determined by the local propagation medium characteristics: the density ρ and the elasticity E ,

$$c = \sqrt{\frac{E}{\rho}}. \quad (1)$$

In sea water, c varies between 1450 and 1500 m/s, depending on salinity, temperature, pressure and pH (as a remainder, acoustic wave propagation velocity in air is approximatively 340 m/s).

The frequency usable for a particular underwater sonar application is constrained by the sound wave attenuation, which increases very rapidly with frequency and limits the reachable distance (or range). In mine hunting, the frequencies of underwater sonars vary between 0.1 and 1 MHz (and their range between 1 and 0.1 km, respectively).

Underwater sonar is composed of hydrophones, which can transmit and receive acoustic waves or only receive echoes from the underwater. The first case is referred as active sonar and the latter as passive sonar. For the purpose of sea mine detection, active sonar is applied. **Figure 1** shows a scheme of a generic active sonar system. When an hydrophone transmits an

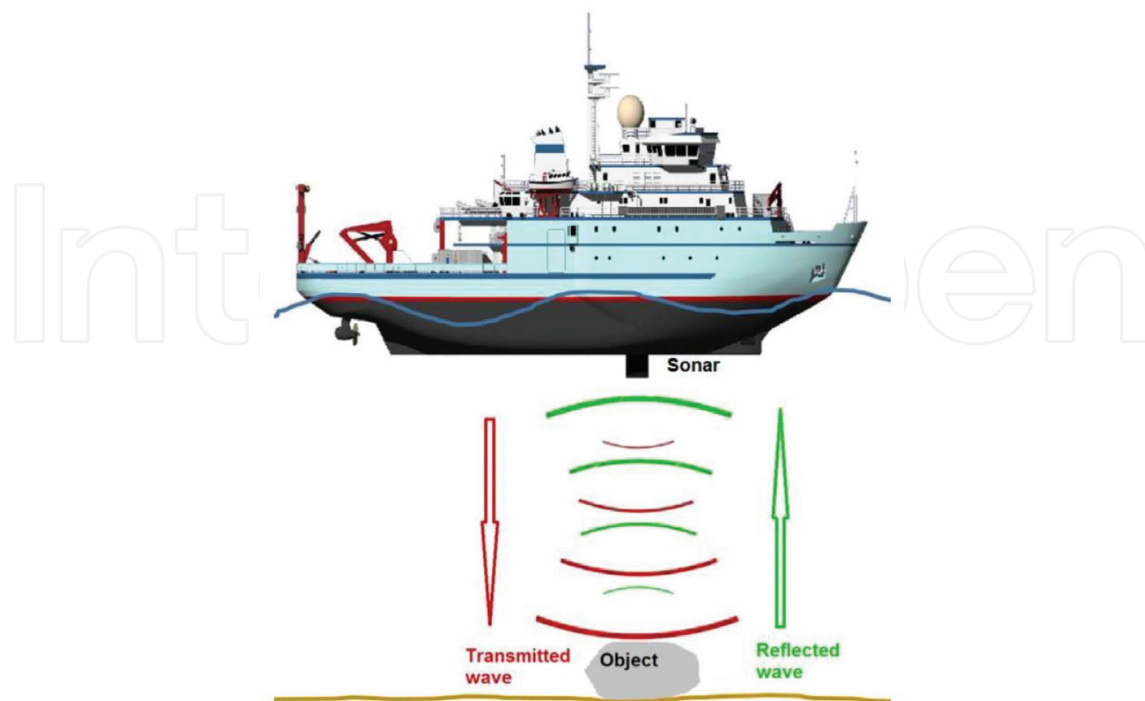


Figure 1. Schematic representation of a hull-mounted active sonar system.

acoustic wave, this propagates underwater and is reflected by any interface with a different characteristic impedance $Z = \rho c$, where ρ is the density of the interface and its unit is Rayl or kg/sm^2 . The reflected wave is then recorded by an hydrophone, and the time delay τ between transmission and reception determines the distance R at which the interface is located, $R = c\tau/2$. **Table 2** lists characteristic impedances of some materials.

The underwater propagation medium is limited by two well-defined interfaces: the sea surface and the sea bottom. Considering the reflection coefficient

$$V = \frac{Z_1 - Z_0}{Z_1 + Z_0} \tag{2}$$

and replacing the values by the impedance of sea water $Z_0 = 1.54 \times 10^6$ and of air $Z_1 = 415$ from **Table 2**, the reflection coefficient is then $V \approx -1$. Therefore, when an acoustic wave hits the sea surface (assumed flat) from below, it is reflected with no change in amplitude and a phase shift of π . A series of multiple paths are generated by unwanted reflections at these two interfaces, and the performance of a sonar system can be highly degraded by these parasite signals [4].

When acoustics waves propagate, the most evident effect is their loss of intensity because of the *geometrical spreading* and *absorption* of acoustic energy by the propagation medium itself. As the transmitted acoustic wave travels over a larger and larger surface, its intensity decreases proportionally to the inverse of the surface (geometrical spreading loss). Additionally, the acoustic pressure decreases exponentially with distance as part of the transmitted wave energy is absorbed by sea water through viscosity or chemical reactions [4].

There are other aspects associated with the propagation of acoustic waves in sea water that are not introduced here, since it is not the scope of this chapter. For more information, the interested reader should refer to Ref. [4].

3.2. Imaging the sea bottom using synthetic aperture sonar

Acoustic imaging is an inverse problem where the goal is to construct an image which represents the locations of discrete targets. This image results from the estimation of the reflectivity (or backscattered acoustic energy) for all ranges and in all directions. In sonar, it is common

Material	Characteristic acoustic impedance (in Rayl)
Air	415
Sea water	1.54×10^6
Clay	5.3×10^6
Sand	5.5×10^6
Sandstone	7.7×10^6
Granite	16×10^6
Steel	47×10^6

Table 2. Some materials and their characteristic acoustic impedance.

to have a horizontal array of receiver hydrophones. The azimuth (or along-track) resolution is given by the array length measured in wavelengths. The range resolution is given by the bandwidth of the system. The along-track resolution can be increased either by increasing the array length or by increasing the frequency. As very large arrays are impractical, the along-track resolution is usually improved by increasing the signal frequency. However, high-frequency signals suffer from attenuation and will therefore limit the application to shorter ranges. This reduces the area coverage rate and makes the sonar impractical for surveying large areas. A solution (adapted from radar) is to use synthetic aperture processing, where successive sound pulses (or pings) are coherently combined to synthesize a longer array. An excellent introduction to synthetic aperture sonar (SAS) can be found in Ref. [5].

Figure 2 shows the acoustic image (in grey scale) of an area of the Belgian continental shelf surveyed using the ROV SHADOWS. SHADOWS is a SAS which works in the range of 100–300 kHz, depending on the mode of operation, and it can achieve a resolution of $5 \times 5 \text{ cm}^2$. It has two horizontal arrays (lateral sonars) of 36 receiver hydrophones each, one located at the port side and the other at the starboard (see **Figure 3**). The length of the arrays is 192.5 cm and that of the SHADOWS platform is 220.6 cm. In order to gather data, SHADOWS is towed at the back of a vessel (in this case, at the back of the oceanographic research vessel BELGICA, or RV BELGICA [6]). Data in **Figure 2** were collected by moving the platform following several lines (or tracks) from south-west to north-east and back at

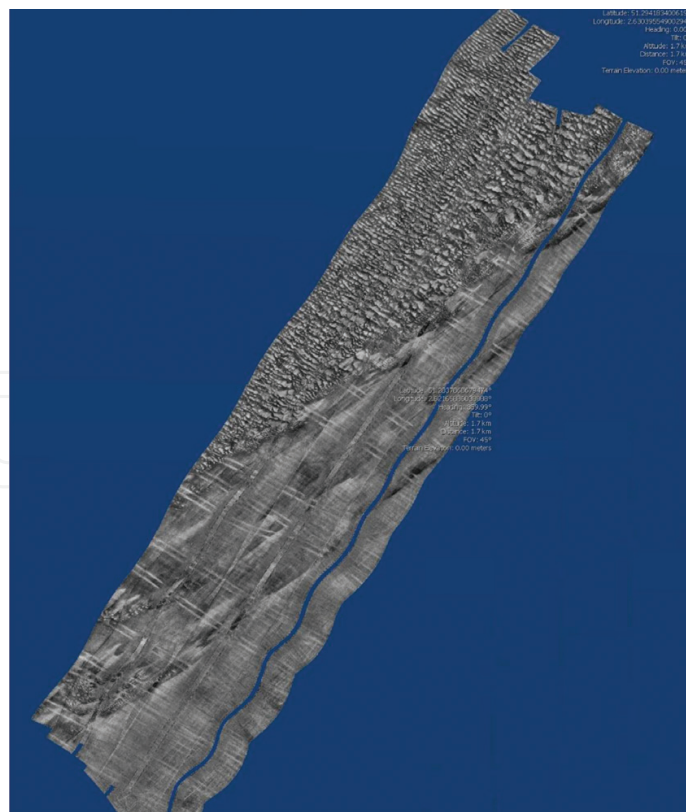


Figure 2. Image of a surveyed area at the Belgian Continental Shelf using the ROV SHADOWS SAS.

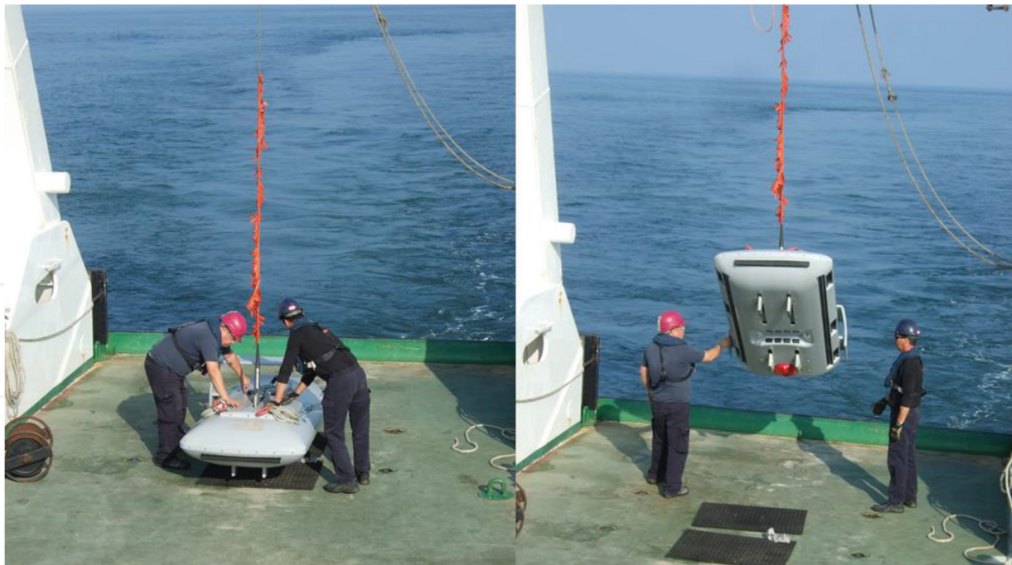


Figure 3. The ROV SHADOWS SAS and its deployment from the RV BELGICA.

an average ground speed of 2 m/s and at an altitude of about 18 m (water column height is 28–30 m). The total covered area is about $2600 \times 700 \text{ m}^2$. In the acoustic image, two main zones with different sea bottom characteristics can be observed. In one part of the image, a rocky and rippled area appears, and it is well differentiated from a second, flatter area. The reflections of some bottom trawling lines across track are also visible. These man-made structures are created by a fishing method which involves a towed bottom fish net or trawl.

3.3. Detection and classification of targets using SAS images

Generally speaking, CAD/CAC and ATR schemas are based on the calculation and extraction of different types of image characteristics, which can mainly be grouped in three categories [7]:

1. Texture-based features, e.g. patterns and local variations of the image intensity.
2. Spectral (or radiometric) features, e.g. colour, energy.
3. Shape-based (or geometrical) features, e.g. length, area.

CAD/CAC and ATR systems developed to classify objects from real aperture or lateral sonar images are generally built on a combination of different features extracted from the spectral highlight response produced by the target and the geometrical characteristics of its shadow on the seafloor. In SAS, since the resolution is improved compared to a real aperture or lateral sonar, more complete geometrical information from the object shadow and highlight (or echo) is available, which could be exploited to improve classification results. Therefore, the approach presented here is based on geometrical features obtained from the increased image accuracy available in both object echo and shadow acoustic responses.

3.3.1. Detection

Before extracting geometrical features, two pre-processing steps are applied: (i) a speckle reduction filter is applied to improve the quality of the image and (ii) a segmentation algorithm is applied to detect echo and shadow pixels from the target. Multiplicative speckle noise is always present in SAS images, which is due to the coherent nature of scattering phenomena from rough interfaces. In Ref. [8], some speckle reduction techniques from synthetic aperture radar images are proposed and developed or adapted to be applied to SAS HR images. Those filters include anisotropic diffusion filter, adaptive neighbourhood and mean adaptive and are compared with other linear and non-linear filters, such as the Lee filter, Kuan filter and a wavelet-based methodology. A performance analysis is carried out considering image quality and better speckle suppression index. Results of the study concluded that the anisotropic diffusion filter was the best choice for this application. Some results after applying anisotropic diffusion and comparison with other filters are presented in **Figure 4**. Data were collected using the MUSCLE AUV from Centre of Maritime Research and Experimentation, NATO Science and Technology Organization (CMRE-STO) during the COLOSSUS measurement campaign along the Elba Island (Italy). MUSCLE AUV is equipped with a 300-kHz interferometric SAS, and it can achieve a resolution of 2.5 cm along track and 1.5 cm across track.

To detect the echo and shadow pixels from the despeckled image, some segmentation techniques are presented and evaluated in Ref. [8]. A rudimentary methodology for segmenting

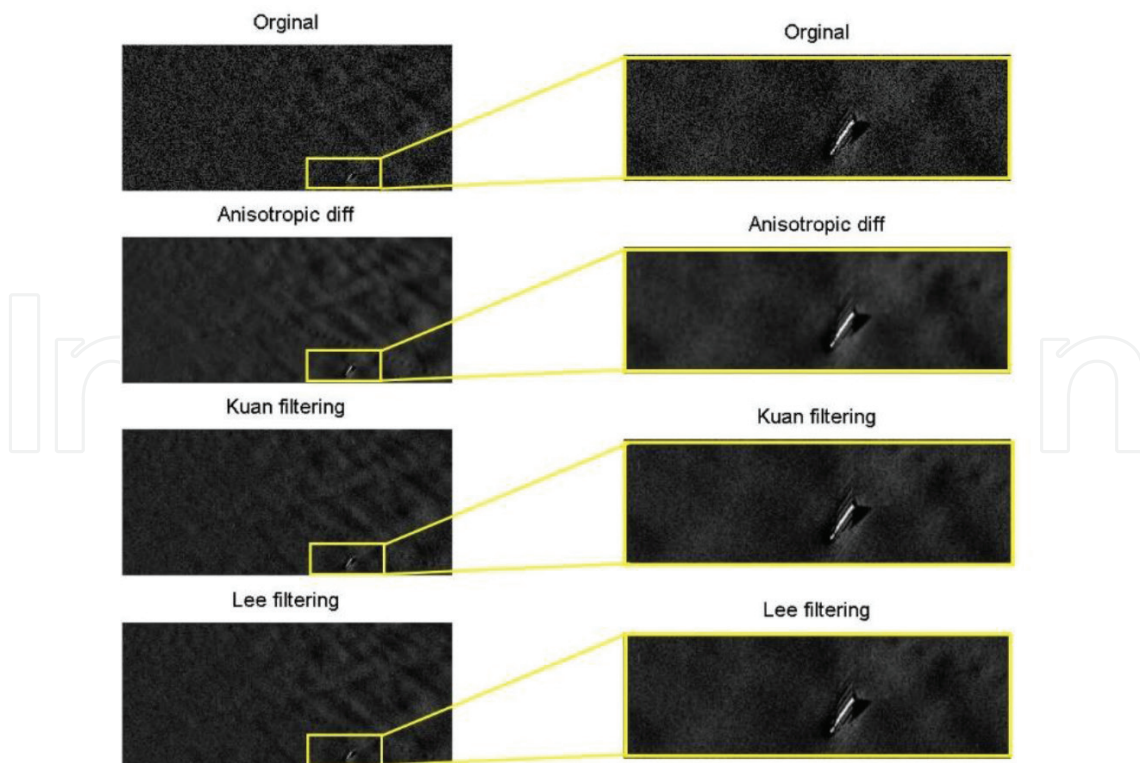


Figure 4. Results after applying different speckle reduction filters to a snapshot of MUSCLE data.

the image is to set an intensity such that all pixels below a level α become part of a mask or class (further referred to as *shadow* and *echo*), while pixels under that level do not. This basic approach has major downsides, notably (i) the selected threshold is frequently not obvious; and (ii) fixing a hard threshold will usually end in resulting masks that are imprecise; first, by the lack of continuity in the algorithm, that is, pixels at level α are part of the class, but that pixels at level $\alpha + 1$ are not, and second, that by not considering the pixel's local area, an important feature is ignored which could perhaps help in the description of the mask itself. Other techniques include Markov random fields to approach the differing grey level zones and the pixel correlations within the zones, and statistical snakes, which uses a closed curve that segments the image into an object area and the surroundings. Although these two methodologies give a good division procedure, they require iterative, computationally expensive calculations, especially when processing large datasets as it is the case here. Therefore, a segmentation method that creates a soft threshold based on fuzzy sets and takes into account the pixel's neighbourhood intensity level presented in Refs. [8, 9]. In fuzzy sets, the degree of membership μ_A to a segment A is distributed into the unit interval $[0, 1]$, with values close to 1 implying a higher degree of membership. In this case, the degree of membership of a given pixel to one of the classes taken into account here (shadow or echo) is described by using a fuzzy set whose membership function is calculated using the pixel's intensity value i and the pixel connectivity value c . In the case of the shadow class, an adequate degree of membership is presented in Ref. [9] as

$$\mu_i = \begin{cases} 1 & \forall i \leq \alpha \\ e^{-(i-\alpha)^2/2\sigma_i^2} & \text{otherwise} \end{cases} \quad (3)$$

where α is an original threshold, and σ_i is the standard deviation of the distribution. The variable σ relates the 'speed' at which the membership decays for $i > \alpha$. Higher values of σ show a tendency to include more pixels as part of the shadow, and lower values show a tendency to refuse more.

This membership function μ_i is integrated following the Boolean logic function AND with a membership function based on the pixel connectivity. Connectivity is computed by convolving the image describing the current shadow class (an image where pixels belonging to the current shadow having a value of 1 and 0 elsewhere) with a kernel $n \times n$. One example of this kernel can be an ones- 3×3 matrix $\begin{bmatrix} 1 & 1 & 1 \\ 1 & 1 & 1 \\ 1 & 1 & 1 \end{bmatrix}$. The membership function is then defined as

$$\mu_c = \begin{cases} 1 & \forall c \geq \beta \\ e^{-(c-\beta)^2/2\sigma_c^2} & \text{otherwise} \end{cases} \quad (4)$$

where c is the number of pixels in its immediate neighbourhood which are shadow pixels, σ_c is the standard deviation of the distribution and β is the maximum number of convolutions determined by the kernel.

The next processing level uses morphological filtering. The latter is described by two functions, opening and closing, which are based on two tasks, erosion and dilatation. Imaging a structure S and a kernel k , the erosion of S by k can be expressed as the group of pixels approached by the centre of k when k moves inside S . The dilatation of S by k can be defined by the group of pixels contained in k when the centre of k moves inside S . The opening of S by

k is calculated by the erosion of S by k followed by dilatation of the remaining form by k . The closing of S by k is calculated by the dilatation of S by k followed by erosion of the remaining form by k .

For classification purposes, synthetic data are needed in order to train the algorithms. SIGMAS (Synthetic Image Generator for Modelling Active Sonar) simulator is used to generate the training data. SIGMAS has been developed by CMRE-STO and allows the generation of SAS test sets for arbitrary target models, including mine-like objects (MLO) and friendly objects (FO). SIGMAS also includes bottom topography effects such as ripples, sea bottom slope variations and partial burial of targets [7]. Results for the segmentation approach applied to both synthetic and real data can be seen in **Figures 5** and **6**, respectively.

3.3.2. Classification

Three regions are considered for the feature extraction. Two of them (shadow and echo) have been already calculated following the *fuzzymorpho*-technique described before. The third selected region is the area in between the two previous classes, which corresponds to a low-backscatter area, i.e. the area in the sonar image between the shadow and the echo classes. The features are then calculated as function of some characteristics of the segmented region, such as along and across track region length, the area of the region, and the ellipsoid fitted to the region. It is important to mention that in order to benefit from these three areas, high-resolution images are needed. For images where the echo and low-backscatter areas are just a few pixels large, these characteristics could not be pertinent. If this is the case, characteristics from the shadow region are more likely to be used.

Since there is a large set of features for this application, an appropriate methodology to classify the detected target signatures could be the Markov Chain Monte Carlo approach (MCMC).

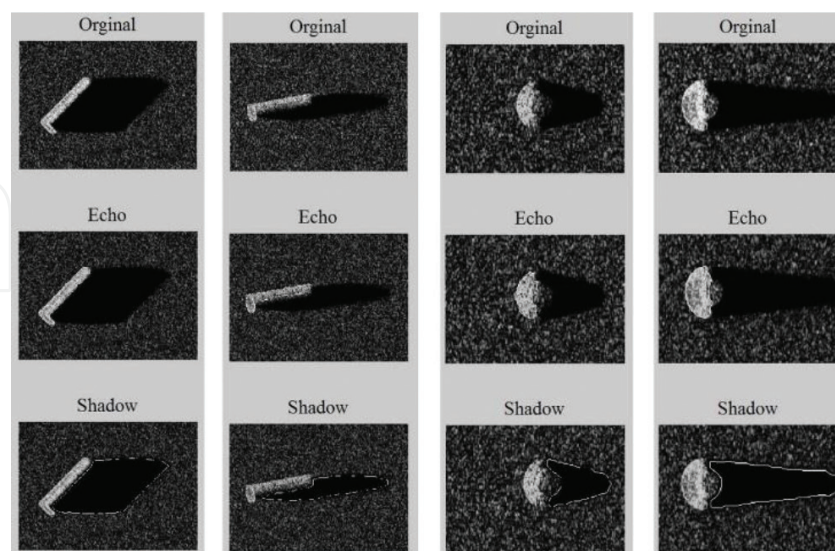


Figure 5. Segmentation of echo and shadow pixels performed on synthetic data for a cylindrical (left) and truncated cone (right) MLOs. Two angles at the same range are shown for the cylindrical MLO and two ranges are shown for the truncated cone.

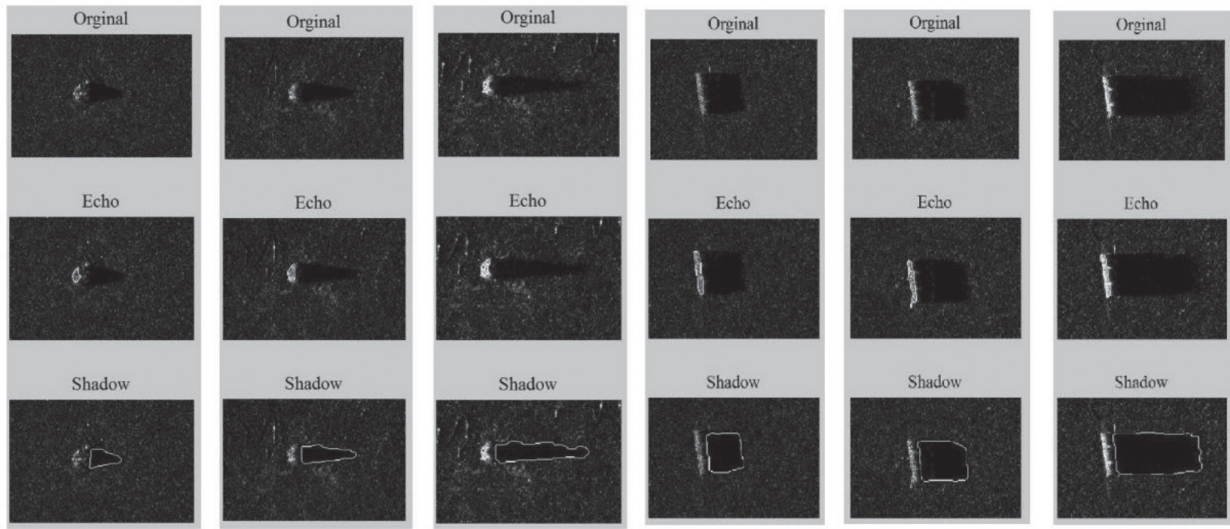


Figure 6. Segmentation of echo and shadow pixels performed on real data for a truncated cone (left) and a cylindrical (right) MLOs at different ranges.

An MCMC simulation is applied to list the parameters from the most indicative ones down to the less revealing ones, according to their discriminative power across distinct classes of data. This is realized by establishing as an importance criterion, the accuracy, obtained using the specific parameters as inputs in the classifier model.

Considering a training set T which consists of a number N of objects (regions of interest, ROIs) $O_{i,j}$ $i = \{1, \dots, N\}$ of class j , $j = \{1, \dots, M\}$. Each object is parameterized by a feature vector of size K , that is, $O_{i,j} = (f_{i,j,1}, f_{i,j,2}, \dots, f_{i,j,K})$. These characteristics would be used to select suitable ways to differentiate between distinct classes. The feature vector is assumed as a succession of variables such that the next value of the succession is only determined by the previous one. Let us examine successive characteristics $f_{i,j,k+1}$ and $f_{i,j,k}$. The characteristic $k+1$ is distributed according to $P(f_{i,j,k+1} | f_{i,j,k})$. Then, the observed probability vector connected to object i of class j is $p_j = (p_j[1], \dots, p_j[K])$. These are the 'true' values for the obtained probabilities attached to objects of class j . The methodology for listing the most indicative parameters down to the less revealing ones is as follows:

1. Sample a large number, F , of observations from each observed probability vector resulting from class j . (Samples consisting of distinct characteristics, carefully chosen in accordance with their component probabilities.) Under the assumptions that (i) the feature vectors for different objects are mutually independent, and (ii) the observed feature vectors resulting from each class are well-parametrized by characteristics, the probability distribution of the sample sizes obtained from this sampling are straightforwardly integrated. The symbol $\text{num}_j[k]$ is used to indicate the number of times feature f_k , $k = \{1, \dots, K\}$, which is selected by the sample for class j . The probability expressed in terms of the p -parameters (probability parameters) of selecting these samples is:

$$P(\text{num}_j | p) \propto \prod_{k=1, \dots, K} p_j[k]^{\text{num}_j[k]}, j = 1, \dots, M \quad (5)$$

2. The p parameters are updated (once the number of features of each size for each sample is obtained). This can be done by noting that the random variable $p_j[k]$ is distributed as

$$\gamma_j[k] / \sum_{l=1, \dots, K} \gamma_j[l], \quad (6)$$

with $\gamma_j[1], \dots, \gamma_j[K]$ mutually independent gamma random variables with respective shape parameters, $\text{num}_j[k] + \alpha_j[k]$. Stated another way, we take advantage of the fact that the Dirichlet distribution is similar to that of proportions of gamma random variables whose shape parameters match the above exponents.

3. The MCMC simulation consists in reiterate processing levels 1 and 2 explained before until convergence.

We index the features by assessing an amount of variation $\text{Var}[k]$ for the p 's at each feature k

$$\text{Var}[k] = \sum_{j=1}^M \frac{(p_j[k] - \bar{p}[k])^2}{SD^2}; \bar{p}[k] = \frac{\sum_{j=1}^M p_j[k]}{M}, \quad (7)$$

where SD is a (MCMC-based) measure of the 'noise' in the posterior distribution of the p 's.

In order to measure the dissimilarity of objects, a suitable distance function can be used. Although the common Euclidean distance function is well explained for a set of parameters of subjective dimension, it reveals major limitations with respect to similarity measurement. This is especially the case if the individual parameters of the feature vector are treated as independent from of each other. In some situations (mostly for spatial data), the components of the feature vector may be correlated. Considering this correlation, methodologies that apply a weighted Euclidean distance have been analyzed. It is relevant to mention that the ordinary Euclidean distance may be studied as being a special case of the weighted Euclidean distance, where the similarity matrix is the identity matrix. There is a large number of choices for these similarity matrices containing correlation coefficients between attributes.

An alternative technique based on the MCMC methodology introduced before is proposed in this section. Listing the parameters from the most indicative ones down to the less revealing ones in each MCMC simulation from until convergence results in a discriminative power weight that can be designated to each characteristic. Assuming that the MCMC simulation is reiterated sim times and features were indexed from the most revealing to the less ones by the number of times r_k they were chosen, the equivalent weight of feature k is $w_k = r_k / \text{sim}$. Each attribute weight thus ranges between $[0 \dots 1]$, assigning to a feature a discriminative power. The proposed weighted Euclidean distance is:

$$\text{wD}_{ij} = \sqrt{\left(\sum_{l=1}^k w_l (p_i[l] - p_j[l])^2 \right)}, \quad (8)$$

and can be used as a distance measurement between the observed probability vectors p_i and p_j representing the initial objects O_i and O_j .

Figure 7 shows an example of the classification approach proposed here. We select a certain synthetic image (object) as a query one, and we retrieved the most similar objects from the snapshots selected out of the real data set. The similarity was defined with respect to the weighted Euclidean distance of the initial normalized feature vectors. In this figure, a query

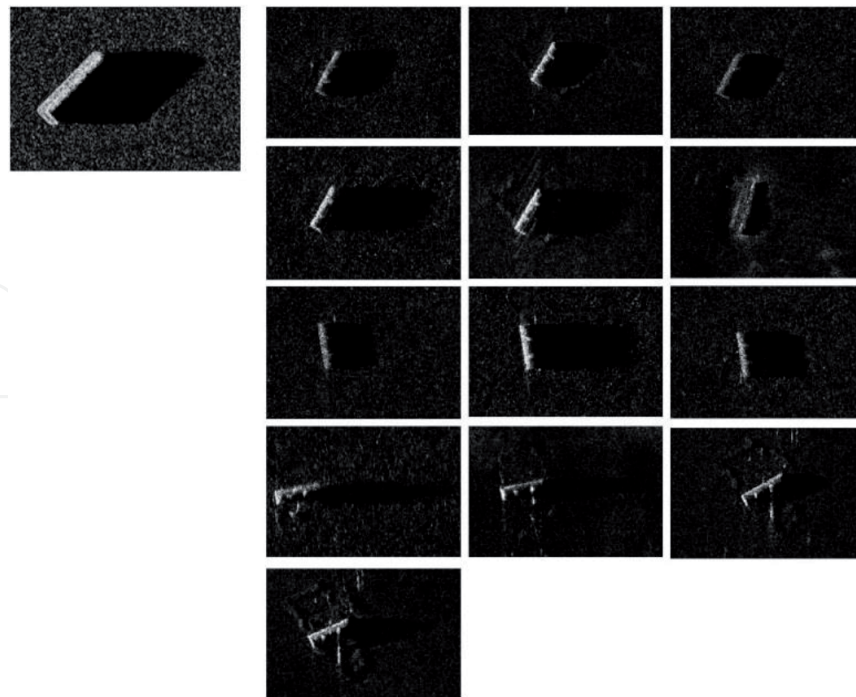


Figure 7. A query object (up, left) and the corresponding retrieved ones using the MCMC-based proposed approach.

cylindrical object is shown in the upper left corner followed by the corresponding retrieved ones from a COLOSSUS data subset. Note that the recovering system (metallic bars attached to the body of the dummy mine) can be easily recognized in the sonar images (four last cropped images in **Figure 7**). This means that the reflected signature (echo) is distinguished as well, having an influence on the classification results. Despite the fact that such objects are designated as cylinder-like, their similarity values are rather lower than the values calculated for the other targets. There is still some analysis to do regarding this effect.

It is important to note that the approach presented here does not transform the initial feature domain into a complicated set of characteristics, and therefore, it is very useful for the mine-hunting application, where both classification accuracy and indicative feature dependencies are important.

4. Magnetic gradiometry applied to mine hunting

Bottom mines can be challenging to detect since they can be buried in the sediment or in the sand. Since sea mines usually contain magnetic materials, a possible technique to detect them is to use a magnetic detector. Several kinds of magnetic detectors can be used to detect sea mines. Total field magnetometers measure the magnetic field magnitude; they can be used to detect dipole targets [10]. Three axis magnetometers measure the three magnetic field vector components and can be applied to mine hunting [11]. The same is true for tensor gradiometers which measure the gradient of the magnetic field [12]. We here consider a total-field gradiometer. It is composed of three total field magnetometers which measure the magnitude

of the magnetic field with a sensitivity of 0.01 nT. The gradiometer is towed behind a ship, and its measurements are used to calculate an estimation of the gradient of the magnetic field magnitude.

A mine can be modelled as a dipolar magnetic source. In this section, a new technique is presented to localize and characterize bottom mines based on a dipolar model. Experimental results achieved in the bay of Gdansk in Poland are also presented.

4.1. The magnetic gradiometer

A sketch of the gradiometer is presented in **Figure 8**. The considered gradiometer is composed of three magnetometers: starboard, port and down, separated by distances $L_{\text{trans}} = 1.5$ m and $L_{\text{vert}} = 0.75$ m. They measure the magnitude of the magnetic field $|\vec{B}_s^i|$, $|\vec{B}_p^i|$ and $|\vec{B}_d^i|$ at N different locations $\vec{r}^i = (x^i, y^i, z^i)$, $i \in \{1, \dots, N\}$. From these measurements, it is possible to compute an estimation of the gradient of the magnetic field magnitude:

$$\begin{pmatrix} G_{\text{trans}}^i \\ G_{\text{long}}^i \\ G_{\text{vert}}^i \end{pmatrix} = \begin{pmatrix} \frac{|\vec{B}_s^i| - |\vec{B}_p^i|}{L_{\text{trans}}} \\ \frac{|\vec{B}_s^i| + |\vec{B}_p^i| - |\vec{B}_s^{i-1}| - |\vec{B}_p^{i-1}|}{2|\vec{r}^i - \vec{r}^{i-1}|} \\ \frac{|\vec{B}_s^i| + |\vec{B}_p^i| - 2|\vec{B}_d^i|}{2L_{\text{vert}}} \end{pmatrix} \quad (9)$$

This is only an approximation since the components of the gradient are calculated by finite differences. This vector can be expressed in an absolute reference frame by multiplying by a rotation matrix:

$$\vec{G}^i = \begin{pmatrix} G_x^i \\ G_y^i \\ G_z^i \end{pmatrix} = \Omega^i \begin{pmatrix} G_{\text{trans}}^i \\ G_{\text{long}}^i \\ G_{\text{vert}}^i \end{pmatrix} \quad (10)$$

The aim of the inversion method is to estimate the magnetic moment \vec{M} and the position \vec{r}_t of the target given the measurements $(\vec{r}^i, \Omega^i, |\vec{B}_s^i|, |\vec{B}_p^i|, |\vec{B}_d^i|)$.

4.2. The inversion method

Traditionally, magnetic targets are localized by looking at the maxima of the magnitude of the gradient [10]. This is achieved by producing a map of this quantity. This method is not optimal because a single target can exhibit several maxima at low latitude. Some interpolation artefacts are also often present, leading to ambiguous interpretation. Moreover, it does not provide precise information about the burial depth or the magnetic moment, which can be used to reduce the false alarm rate [14]. We propose an alternative method for the localization of the target. Instead of producing a map, we directly use the raw data collected by the gradiometer and inverse the dipole model of the field. This allows for a real-time detection. Our method also provides the magnetic moment of the target and its depth. It works regardless of the latitude.

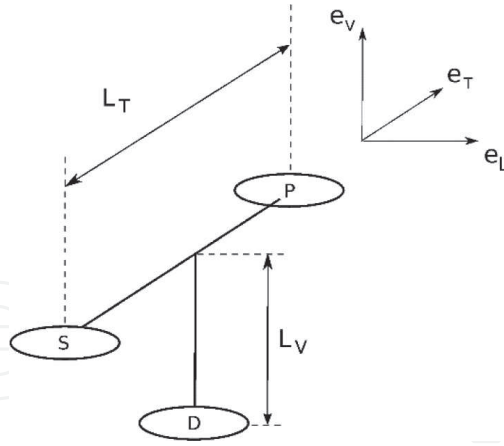


Figure 8. The considered gradiometer is composed of three magnetometers.

4.2.1. Large distance approximation

The gradiometer measures a finite difference approximation of the gradient. If the distance between the gradiometer and the target is large compared to the size of the gradiometer, this approximation will be satisfying. This allows one to estimate the position of the target by solving a linear system of equations. This is called the Euler method.

We assume that the magnetic field measured by the magnetometers has two contributions: the earth's magnetic field \vec{B}_e and the field due to a dipole target \vec{B}_t^i :

$$|\vec{B}^i| = |\vec{B}_e + \vec{B}_t^i|, \quad (11)$$

where

$$\vec{B}_t^i = \frac{\mu_0}{4\pi} \frac{3\vec{R}^i(\vec{M} \cdot \vec{R}^i) - |\vec{R}^i|^2 \vec{M}}{|\vec{R}^i|^5}, \quad (12)$$

and

$$\vec{R}^i = \vec{r}^i - \vec{r}_t. \quad (13)$$

The anomaly field is defined as $A^i = |\vec{B}^i| - |\vec{B}_e|$. If the earth's magnetic field is large compared to the field of the target, it can be shown that the anomaly is given by the projection of the field due to the target on the direction of the earth's magnetic field:

$$A^i \approx \vec{B}_t^i \cdot \frac{\vec{B}_e}{|\vec{B}_e|}. \quad (14)$$

A function $f(r)$ is said to be homogeneous of degree k if $f(\lambda r) = \lambda^k f(r)$, $\forall \lambda > 0$.

A homogeneous function of degree k follows the Euler's homogeneity equation:

$$\vec{r} \cdot \vec{\nabla} f(r) = k f(r). \quad (15)$$

One can easily see that if $|\vec{B}_t^i| \ll |\vec{B}_e|$, the anomaly field is a homogeneous function of degree -3 of \vec{R}^i . The Euler's homogeneity equation takes the form

$$\vec{R}^i \cdot \vec{G}^i = -3 \left(|\vec{B}^i| - |\vec{B}_e| \right). \quad (16)$$

This forms a first linear system of equations that allows to estimate the position of the source. This system can be solved by the linear least mean square method which does not require any initial parameters.

Once the position is known, one can estimate the magnetic moment by solving another linear system. Indeed, Eqs. (12) and (13) show that the anomaly is a linear function of the magnetic moment, and the magnetic gradients are also linear in M . Eq. (10) forms a second linear system of equations that can be solved by the linear least mean square method.

In practice, the hypothesis that the gradiometer measures the true gradient can be a bad approximation at small distance from the target. Estimating the parameters with the linear method leads to inaccurate results, even without noise. Therefore, a more general method is developed and presented here.

4.2.2. General case

Eqs. (11) and (12) can be injected in Eq. (10) to give a system of equations that are nonlinear in terms of \vec{M} and \vec{r}_t .

This nonlinear system of equations can be solved by the Levenberg-Marquardt algorithm that finds the solution of the least mean square problem. This method is iterative and requires good initial parameters to avoid problems of local minima. We take the output of a linear method as initial values.

Figure 9 shows a comparison of the different localization techniques in the absence of noise on the basis of simulations. It allows one to compare the localization accuracy of the map

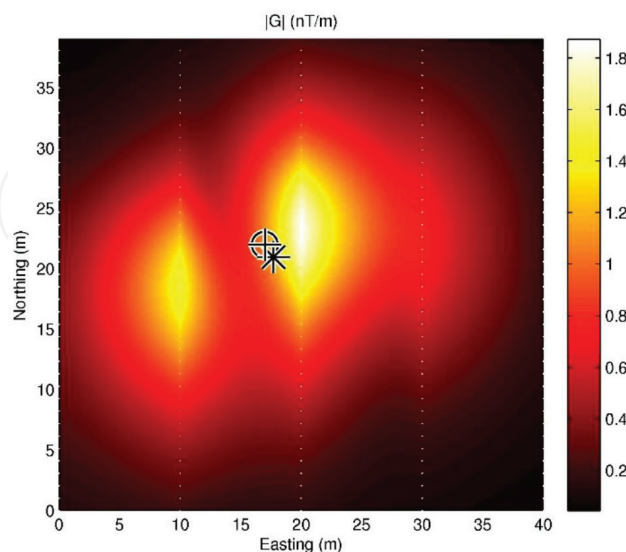


Figure 9. Comparison of the different localization methods. The map represents of the simulated magnitude of the gradient due to a dipole target. The map is produced on the basis of synthetic data taken on five tracks separated by a distance of 10 m. The circle is the true position of the dipole. The star is the position found with the linear method and the cross is the position found with the nonlinear method. The location is best estimated with the nonlinear method.

method, the Euler method and the nonlinear method. The nonlinear method provides the best results.

The effect of the noise on the precision of the estimated parameters is discussed in Ref. [15].

4.3. Experimental results

Some experiments were carried out in the bay of Gdansk, Poland, in September 2015. Two dummy bombs (T_1 , T_2) and four reference targets (T_3 , T_4 , T_5 , T_6) containing magnets of 67 Am^2 were placed at different burial depth as well a magnet of 30 Am^2 (T_7). **Figure 10** is a picture of the system during recovery from sea trials. **Figure 11** shows the signal due to the target T_4 . **Figure 12** shows the positions of the targets measured acoustically after their positioning compared to the positions estimated from the gradiometer measurements together with the map of the gradient magnitude. The root mean square errors are $\Delta_x = 4.3 \text{ m}$, $\Delta_y = 3.1 \text{ m}$ and $\Delta_z = 2.3 \text{ m}$. The main limitation to the target localization accuracy is the accuracy of the gradiometer localization. The reference targets are detected several times, allowing for an estimation of their magnetic moment. The mean estimated magnetic moment magnitude of targets T_3 , T_4 , T_5 and T_6 is of 100 Am^2 to be compared to 67 Am^2 . The smallest detectable magnet was of 30 Am^2 . The main limitation to the detection of smaller targets is the noise level. Those preliminary results have to be refined but are already promising. Better gradiometer localization accuracy and smaller noise level should be reachable, and thus better target localization accuracy and detection performances should be reachable.

4.4. Partial conclusions

The original inversion method developed to retrieve the position and the magnetic moment of a dipole target from magnetic gradiometer measurements works regardless of the latitude, and it can be performed in real time. The knowledge of the horizontal position is important for the localization of the target and the knowledge of the burial depth and the magnetic moment can be used to reduce the false alarm rate. The method is tested on the basis of real



Figure 10. The gradiometer was attached to a platform with remotely controlled depth/altitude. The system was towed behind a boat. This picture was taken by TNO.

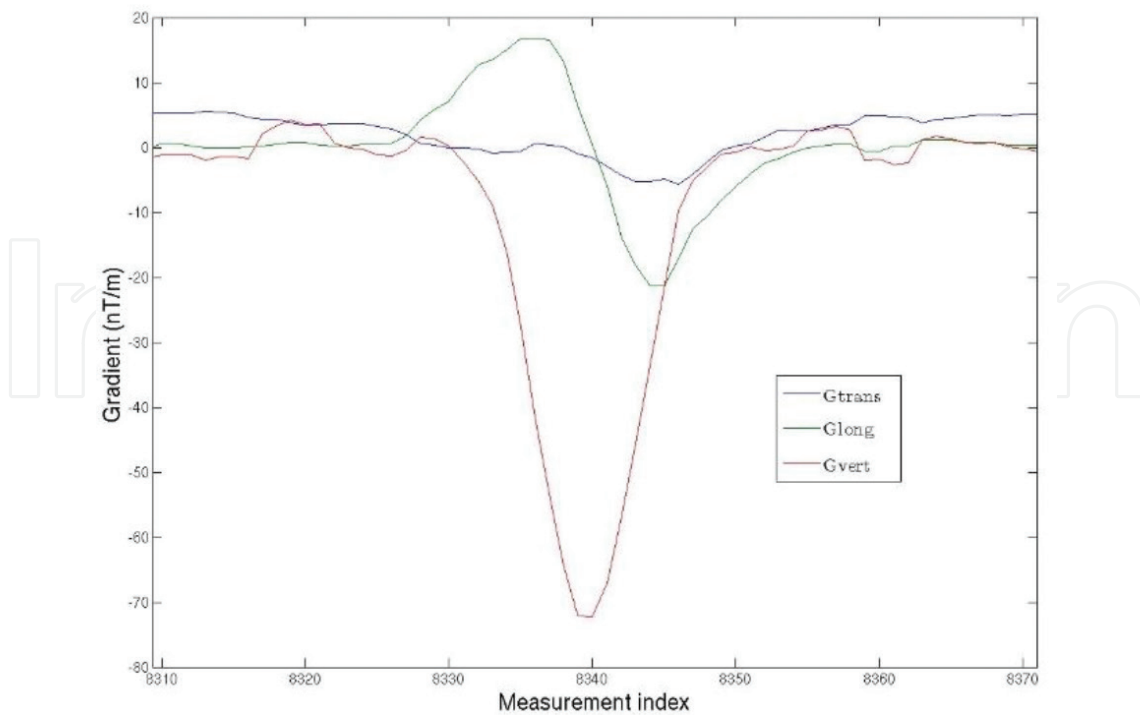


Figure 11. Signal collected by the gradiometer at the vicinity of the target T4.

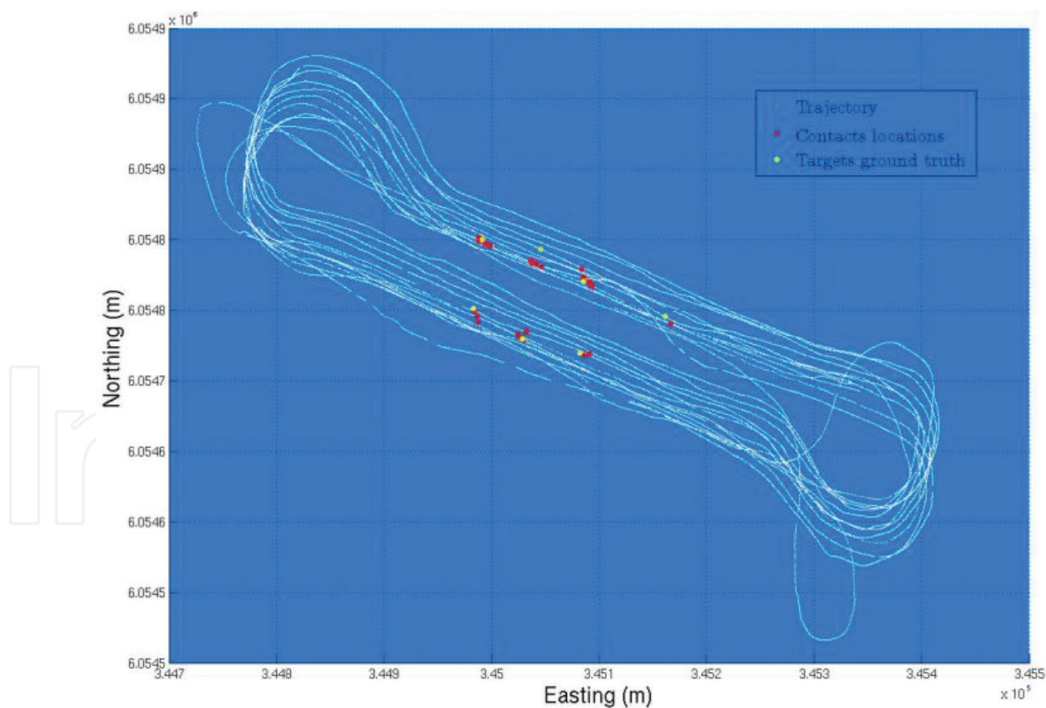


Figure 12. Targets positions (lighter dots) and position estimated on the basis of the gradiometer measurements (darker dots) together with the platform trajectory.

measurements and shows promising results. Further refinements need to be done and an analysis of the noise should allow for the computation of the target presence probability distribution and for data fusion with other sensors.

5. Behaviour-based detection of drifting mines

The threat of untethered drifting sea mines became apparent during the Gulf War of 1990–1991 between Iraq and the international coalition lead by the US. International regulations impose that floating sea mines have to be moored in place, and supplied with a self-disarming mechanism in case anchoring fails. Most nations, even those against international regulations, are inclined to follow these laws, since a buoyant mine carried by random currents is a very inefficient weapon, and could promptly leave the battle area.

Nevertheless, when the hostilities take place in more limited areas with several crafts navigating through, the damage probability rises significantly and floating sea mines can be transformed into a very effective anti-ship weapon. An example of such a region is the Persian Gulf, where a large number of sea mines drifting freely were found by the coalition forces during the Gulf War.

The efficacy of this military tactic was evident when US Navy's amphibious assault carrier Tripoli was brought to a standstill by a sea mine. After this incident, floating sea mines were classified as a principal menace to US Navy aircraft carriers. As a result, warfare was considerably decelerated and risk-reluctant shipping companies heavily diminished their number of times they transit in the conflict area.

Since then, floating sea mines have continued to show up, as recently as during the NATO intervention in Libya in 2011. A similar concern has arisen from the recent terrorist threat: floating IEDs released within a commercial harbour could cause tremendous economic damage, though no such cases have emerged until now.

5.1. Detection methods

Conventional subsurface mines are mainly detected through sonar techniques. This proved inadequate for spotting floating mines; on the one hand, due to the practical matter of downward sensor inclination and on the other hand, because of the cluttered background caused by the active sea surface. The same applies above water: the target is small and partially submerged, and the sea surface acts as a dynamic background hiding the target. In practice, the only reliable detection method so far proved to be a human visual detection and identification. Therefore, an automated detection system would provide a huge benefit in military campaigns, in clean-up operations and even for a number of civilian applications such as collision avoidance, salvaging and search and rescue.

The conditions required here are for a ship-based system to be able to operate 24 hours a day and in different weather conditions. Although the diameter of the expected targets is rather limited, it has been demonstrated that it is possible for a human operator to visually detect the target. Therefore, an infrared video imager is selected for this application.

Automated detection of the floating mine is hard, because waves on the sea surface are similar in size, shape and thermal emissivity as a partially submerged floating mine in thermal equilibrium with the water. This makes even advanced background subtraction methods such as

EGMM¹ and ViBE² [13], which are capable of dealing with significant amounts of noise in the image, unsuitable for detecting objects on the dynamic scene presented by the sea surface [14].

A better feature to discriminate between object and background is the motion behaviour of the dynamic elements in the scene. Waves propagate in a linear fashion across the scene along the wind direction, whereas the drifting mine shows a vertical oscillation and a slower drift with the subsurface current (not necessarily along the wind's vector). Both may change shape and appear/disappear, complicating matters.

Different target-based tracking techniques, e.g. mean-shift tracking [15] and particle filters [16], could be applied to create a background motion model. The latter could be useful when classifying object tracks as foreground or background. Essentially, the main disadvantages of these approaches are dealing with the large quantity and high variability of the dynamic background targets, and with the restrained target information delivered by infrared image arrays [17]. Optical flow [18] and block-matching [19] techniques have been applied with promising results. Besides, real-time performance is needed in order to make this application useful, and therefore, algorithms operating at the pixel level are preferred here.

5.2. Behaviour subtraction

The method we describe here is the behaviour subtraction method [14] first described in Ref. [20]. This is a pixel-based method in which behaviour signatures over a time window are evaluated and compared to a learned background model. It is fairly simple, computationally quick and easily extended to use multiple features. We will continue to describe this method in the following sections.

The behaviour subtraction method has at its core the idea that one should look at events in a video sequence, not at objects in individual frames. Then, the features of these events can be extracted, analysed, used to construct a background model and to detect outliers to that background model.

For this, activity in the scene needs to be detected first. The background subtraction methods mentioned earlier provide us with the necessary tools for this: they detect change in the image on a per-pixel level. Now, while state-of-the-art background subtractions such as EGMM or ViBE try to minimize unnecessary detections, we actually prefer having lots of events. This, and computational simplicity, is why typically a very simple running mean background subtraction is used.

Background subtraction converts the video stream into a stream of binary activity images, where pixels contain the value 1 if change was detected (and hence an event is occurring) or 0 if not. When we look at a set time-window's worth of these, each pixel will be characterized by a behaviour signature, a sequence of 0's and 1's describing the activity in this scene. From this, a number of simple activity features can be extracted [21, 22]:

¹Extended Gaussian mixture model.

²Visual background extractor.

- The total activity in the time window, summing all of the activity bits in it and giving a general measure of the event's 'business' in that pixel.
- The number of transitions between activity and nonactivity, giving us some form of frequency information.

These two measures are ideally suited for the drifting mine problem, as both generic movement behaviour and frequency are deemed characteristic features distinguishing between the mine and the surface waves.

The next step in behaviour subtraction is the construction of a background model and a method for detecting outlier behaviour. A probabilistic approach is possible [23], but a more pragmatic and computationally simpler method is possible. For this, behaviour features are calculated for a set of training data. If we just look at one behaviour feature, say the total activity in a time window of set length, for each pixel, we can find the maximum value of the said feature. The resulting image will be called the behaviour image representing the background model.

Outlier detection then simply becomes calculating the online behaviour image at time t , subtracting the trained background model from it and thresholding the result, as can be seen in **Figure 13**; hence, the name behaviour subtraction.

5.3. Validation

In order to validate the performance of the algorithm on actual measurements, we used the Elbit MicroCompass MWIR camera system mounted on the P901 Castor patrol vessel of the Belgian Navy (see **Figures 14–16**). Since policing belongs to the tasks of the ship, recording capability is provided, allowing us to obtain video footage from the infrared camera.

Measurements with this system were done in the harbour where the Castor was at anchor. A small practice mine was released in the dock at a distance of approximately 250 m, and the camera was zoomed out to cover the entire width of the mouth of the dock. This resulted in the target being observed with an object size of about 6 pixels, making detection a hard (but not impossible) task for both a human observer and our detection algorithm.

The mine was released in the middle of the mouth of the dock by a RHIB and let free to be carried by the current. Sea state was approximately 1–2, so unfortunately the amount of wave activity was limited and not representative of tests at sea. Still, the tests provide us with a best-case scenario using an MWIR sensor against which future tests may be compared.



Figure 13. From left to right: IR image, activity image, behaviour subtraction.



Figure 14. P901 Castor patrol vessel.



Figure 15. MicroCompass sensor.



Figure 16. Operator station for the MicroCompass camera on P901 Castor.

Four sequences of video footage of the drifting mine were recorded during these tests, along with a number of sequences of swimmer and small boat activity. **Figure 17** shows a snapshot of one of those videos. Ground truth annotation was performed on the mine sequences for performance evaluation of the detection algorithm.

Video files amount to 10 minutes of footage and are encoded to MPEG-4 format using the H264 codec with a resolution of 720×576 pixels at 25 fps. Compression settings were not accessible, and neither were temperature ranges, but no problematic compression artefacts were observed in the data.

We applied the behaviour subtraction algorithm to these video sequences varying training sets, behaviour features, time window lengths and thresholds, and compared the detection results to the annotated ground truth position of the drifting mine, in order to obtain sets of true positive ratio (TPR) and false positive ratio (FPR) values. These values are plotted and the resulting convex hull provides us with an ROC curve for each parameter set describing the algorithm's performance. The calculated ROC curves can be seen in **Figures 18–20**.

Behaviour subtraction accumulates per-pixel activity features over a sliding time window in order to build up a 'behaviour image' of the scene, which is compared to a prior learned behaviour model in order to detect behavioural anomalies. The two main behaviour features are the activity sum, adding all the pixels in which a background subtraction has indicated that an activity is taking place, and the transition count, in which all of the changes between active and non-active during the time window W are counted.

The size or length of the time window W is one of the defining parameters of the algorithm. We chose to evaluate values of 5, 25, 50 and 100 frames, which given the 25fps frame rate of MicroCompass corresponds to lengths of 1/5, 1, 2 and 4 s. We evaluate the algorithm's performance by plotting the TPR (true positive ratio) and FPR (false positive ratio) pairs for multiple runs of the algorithm with varying thresholds in a graph, and subsequently plot the convex hull enveloping these points. This convex hull is known as the ROC (receiver operating characteristic). When we evaluate the ROC curves for behaviour subtraction using the activity sum feature, we see that the 1- and 2-second time windows outperform the other values. We also immediately see that for these values we obtain a very good ROC curve, approaching ideal performance. In a way,



Figure 17. Drifting mine in the Zeebrugge harbour as captured by the MicroCompass MWIR sensor on the P901 Castor.

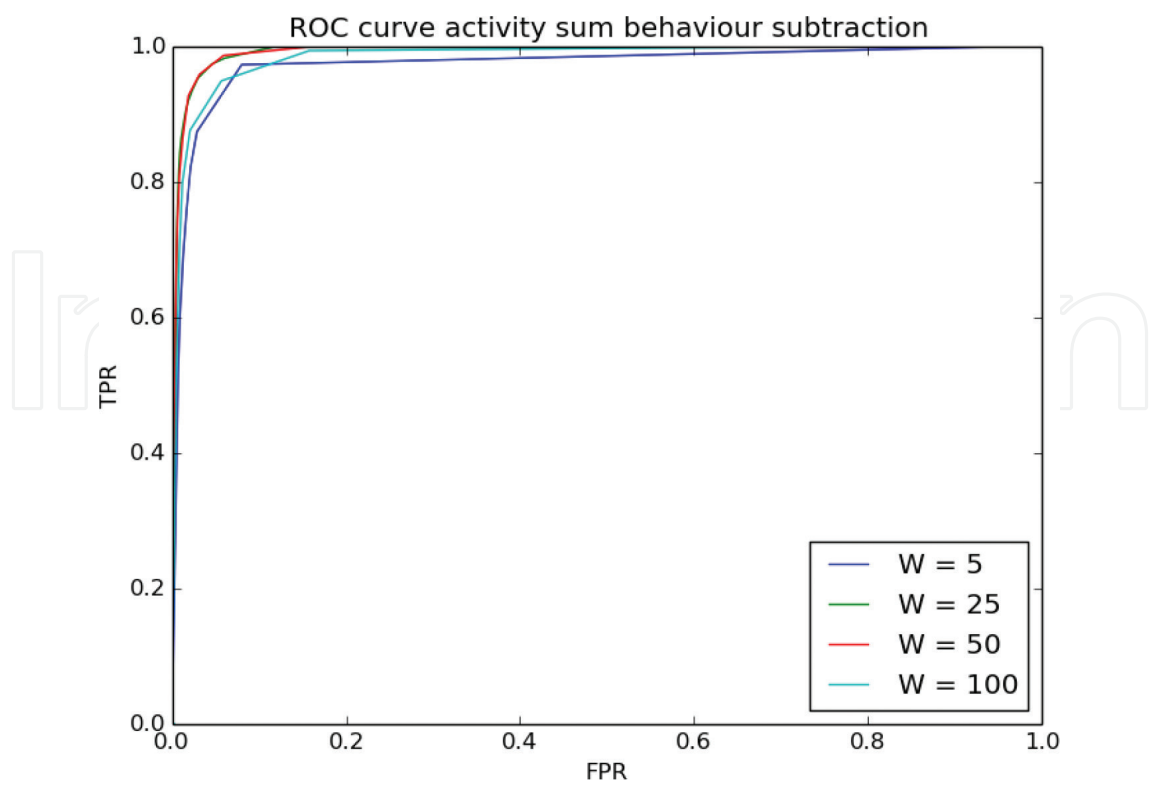


Figure 18. Comparing activity sum performance for different time window sizes.

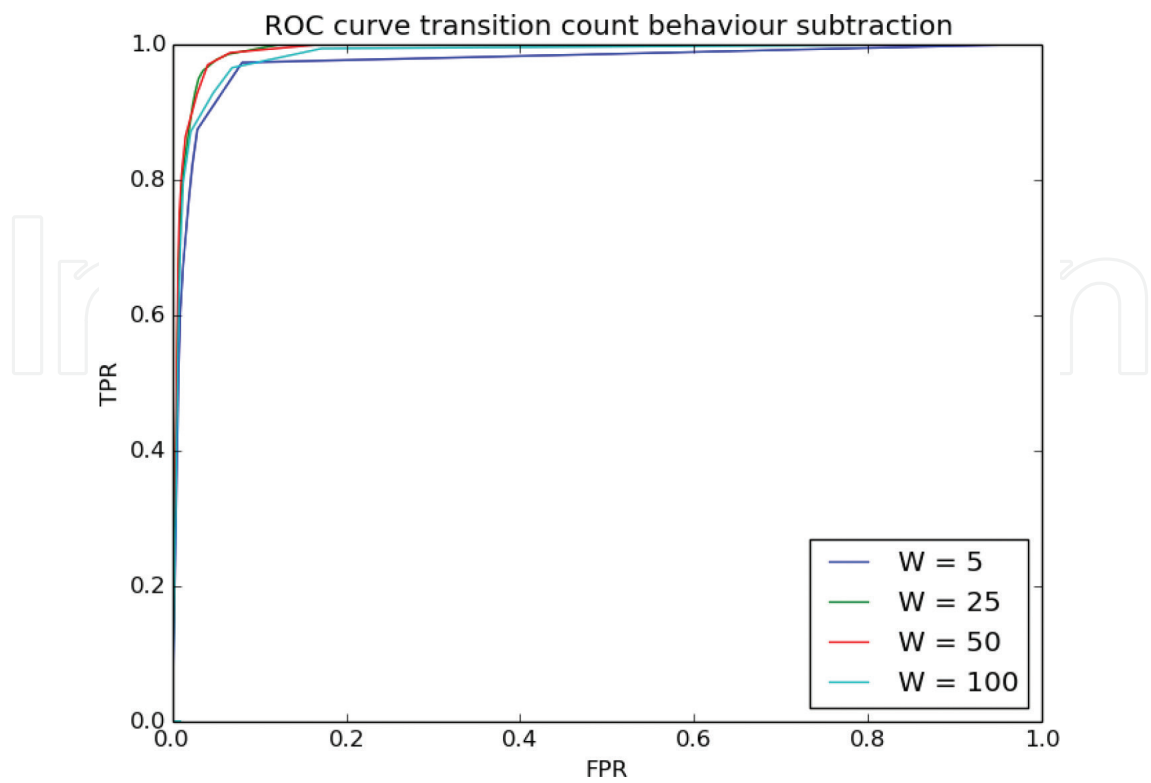


Figure 19. Comparing transition count performance for different time window sizes.

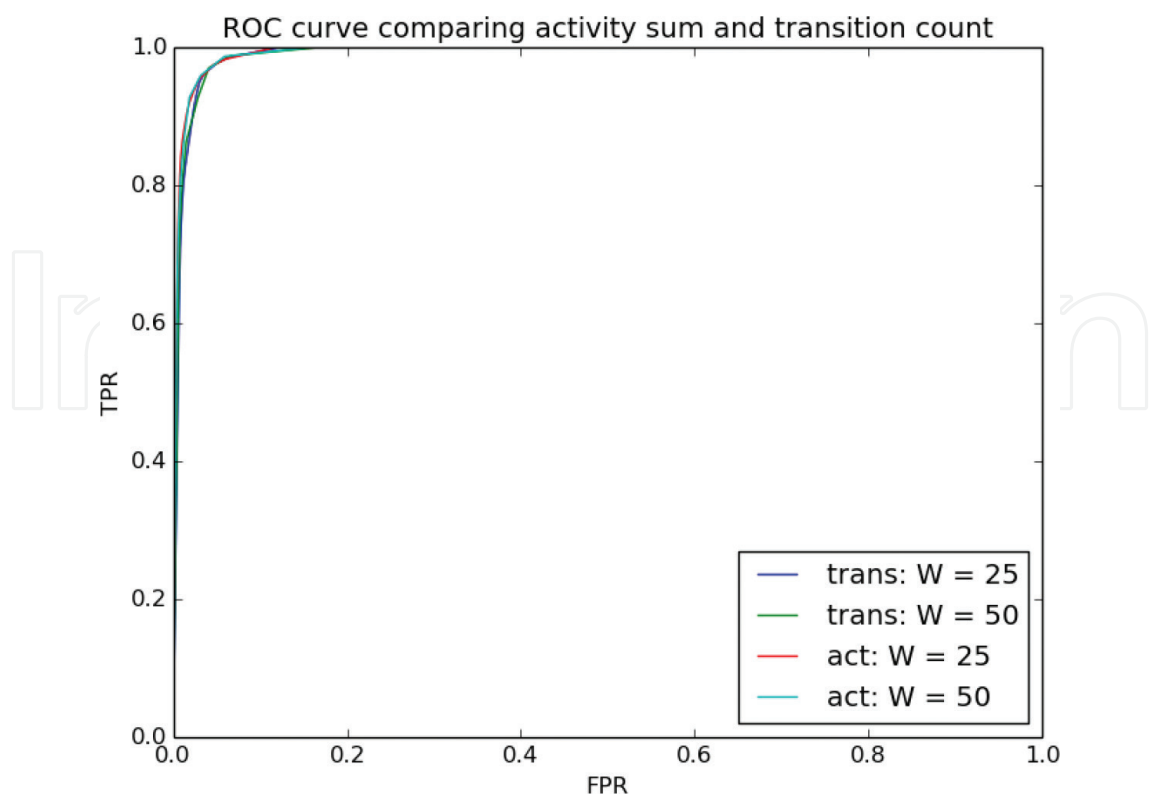


Figure 20. Comparing activity sum and transition count performances.

this was to be expected for the near-ideal conditions for a drifting mine on a sea with sea state 1–2, yet in practice, the mine was not always that easy to spot for a human observer, meaning that the algorithm remains promising.

When we evaluate the transition count feature for the same time window sizes, we obtain very similar results. Both behaviour features perform equally well, something we also see when comparing both in the same plot for the optimal window sizes of 25 and 50 frames.

These results do not allow us to make a choice as to whether the 25- or 50-frame time windows are better suited to the problem. We assume that in higher sea state conditions, the 50-frame window will perform better, but this will have to be determined with additional data.

These results demonstrate that the detection of floating mines (and similar objects) on the sea surface using passive sensors and behaviour analysis is possible. The behaviour subtraction algorithm seems to be an ideal method for the initial detection of floating targets. Further classification procedures can build upon this, with or without human operator involvement.

To implement this as an operational collision avoidance system on a moving ship, we would recommend a scanning setup, in which a stabilized camera system (thermal or optical) scans staggered sections of a designated safety zone for periods of 5–10 seconds.

In future work, we would like to see to what extent behaviour subtraction can be improved by using different or multiple activity features. Furthermore, we would like to validate the method on data obtained at greater distances and higher sea states.

6. Conclusion

Some techniques developed at RMA in order to detect and/or classify sea mines are summarized in this chapter. These techniques include different sensors and apply different advanced signal processing approaches. Due to the complexity of the ocean environment, these techniques have their advantages and drawbacks. Each of the methodologies presented here is focused in a particular type of sea mine, and therefore, they are complementary. Further research should be focused in the integration of these techniques in a MCM system that accomplishes an end-to-end mission from search to disposal using autonomous vehicles. Processing and decision-making capabilities should be integrated on-board of the sensor's vehicles. In order to improve mine hunting capabilities in conditions that are difficult for conventional systems, new sensing modalities should also be investigated.

Acknowledgements

The work related to the sonar is carried out at the Royal Military Academy of Belgium for the Belgian Navy Component, in the scope of research projects MRN09 and MRN17, both funded by the Belgian Ministry of Defence. Ship time on board of the RV Belgica was provided by BELSPO and RBINS-OD Nature. OD-NATURE and the RV Belgica are gratefully acknowledged for outstanding support in collecting SHADOWS data. CMRE is gratefully acknowledged for sharing MUSCLE data through the Joint Research Program MIAMS.

The work related to the gradiometer is carried out at the Royal Military Academy of Belgium for the Belgian Navy Component, in the scope of research projects MRN10 and MRN16, both funded by the Belgian Ministry of Defence. The experiments were done within the EDA UMS BURMIN project, in collaboration with TUS, ATLAS, TNO, CTM, IPHT Jena, Fraunhofer Institute and ECA.

The work related to drifting mines detection is carried out at the Royal Military Academy of Belgium for the Belgian Navy Component, in the scope of research project MRN13, funded by the Belgian Ministry of Defence. The P901 Castor patrol vessel of the Belgian Navy is gratefully acknowledged for outstanding support during the experiments.

Finally, the authors would like to thank Adm Yves Dupont for his help in improving this manuscript.

Author details

Olga Lucia Lopera Tellez*, Alexander Borghgraef and Eric Mersch

*Address all correspondence to: olopera@elec.rma.ac.be

CISS Department, Royal Military Academy, Brussels, Belgium

References

- [1] Morris DA. The Mine Warfare Cycle: History, Indications, and Future. Globalsecurity.org; 1997. Available from: <http://www.globalsecurity.org/military/library/report/1997/Morris.htm> [Accessed: September, 2015]
- [2] Rios JJ. Naval mines in the 21st century: Can NATO navies meet the challenge? [Master's thesis]. Naval Postgraduate School, 2005, pp. 12-16
- [3] US Navy Maritime Mammal Program. Available from: <http://www.public.navy.mil/spawar/Pacific/71500/Pages/default.aspx> [Accessed: September, 2015]
- [4] Lurton X. An Introduction to Underwater Acoustics—Principles and Applications. 2nd ed. Xavier Heidelberg: Lurton Springer; 2010
- [5] Hansen R. In: Kolev N, editor. Introduction to Synthetic Aperture Sonar, Sonar Systems. InTech; 2011. DOI: 10.5772/23122. ISBN: 978-953-307-345-3. Available from: <http://www.intechopen.com/books/sonar-systems/introduction-to-synthetic-aperture-sonar>
- [6] <http://www.howbigisbelgica.be/en/index.php>
- [7] Vera J, Coiras E, Groen J, Evans B. Automatic target recognition in synthetic aperture sonar images based on geometrical feature extraction. EURASIP Journal on Advances in Signal Processing. 2009;1:1-10. DOI:10.1155/2009/109438
- [8] Lopera O, Dupont Y. Combining despeckling and segmentation techniques to facilitate detection and identification of seafloor targets. In: IEEE eProceedings of Oceans, Santander, Spain. December, 2012. pp. 1-4
- [9] Myers V. Sonar image segmentation using iteration and fuzzy logic. In Proceedings on CAD/CAC Conference, Halifax, Nova Scotia, Canada; 2001
- [10] Sheinker A, Shkalim A, Salomonski N, Ginzburg B, Frumkis L, Kaplan BZ. Processing of a scalar magnetometer signal contaminated by $1/f$ α noise. Sensors and Actuators A: Physical. 2007;138(1):105-111
- [11] Sheinker A, Lerner B, Salomonski N, Ginzburg B, Frumkis L, Kaplan BZ. Localization and magnetic moment estimation of a ferromagnetic target by simulated annealing. Measurement Science and Technology. 2007;18(11):3451
- [12] Wynn WM. Detection, localization, and characterization of static magnetic dipole sources. Journal of Detection and identification of visually obscured targets. 1999;1:337-374
- [13] Li X. Understanding 3D analytic signal amplitude. Geophysics. 2006;71(2):L13
- [14] Yvinec Y, Druyts P, Dupont Y. Detection and classification of underwater targets by magnetic gradiometry. In: Proceedings of International Conference on Underwater Remote Sensing, Brest, France. I. Quidu et al. (ed) 2012
- [15] Mersch E, Yvinec Y, Dupont Y, Neyt X, Druyts P. Underwater magnetic target localization and characterization using a three-axis gradiometer. In: Proceedings of OCEANS'14 conference, Taipei, Taiwan; IEEE; 2014

- [16] Barnich O, Van Droogenbroeck M. ViBE: A powerful random technique to estimate the background in video sequences. In: IEEE International Conference on Acoustics, Speech and Signal Processing, 2009. ICASSP 2009. Taipei, Taiwan; IEEE; 2009. pp. 945-948
- [17] Borghgraef A, Lapierre F, Barnich O, Vandroogenbroeck M, Philips W, Acheroy M. An evaluation of pixel-based methods for the detection of floating objects on the sea surface. EURASIP Journal on Advances in Signal Processing. 2010;**2010**:11
- [18] Comaniciu D, Ramesh V, Meer P. Kernel-based object tracking. IEEE Transactions on Pattern Analysis and Machine Intelligence. 2003;**25**:564-577
- [19] Khan Z, Balch T, Dellaert F. An MCMC-based particle filter for tracking multiple interacting targets. In: European Conference on Computer Vision; T. Padjad and J. Matas (ed); 2004, vol. IV. pp. 279-290
- [20] Cheng J, Yang J. Real-time infrared object tracking based on mean shift. Progress in Pattern Recognition, Image Analysis and Applications. 2004;**3287**:45-52
- [21] Borghgraef A, Lapierre FD, Acheroy M. Motion segmentation for tracking small floating targets in IR Video. In: 3rd International Target and Background Modeling and Simulation (ITBMS) Workshop. 3rd ed., Toulouse, France; 2007
- [22] Wei Z, Lee D, Jilk D, Schoenberger R. Motion projection for floating object detection. Advances in Visual Computing. 2007;**II**:152-161
- [23] Jodoin P-M, Saligrama V, Konrad J. Behavior subtraction. IEEE Transactions on Image Processing: A Publication of the IEEE Signal Processing Society. 2012;**21**(9):4244-4255

